PNAS RESEARCH ARTICLE | NEUROSCIENCE

Orientation anisotropies in macaque visual areas

Chen Fang[a], Xingya Cai[a], and Haidong D. Lu[a,1]

Edited by J. Anthony Movshon, New York University, New York, NY; received July 28, 2021; accepted March 10, 2022

In mammals, a larger number of neurons in V1 are devoted to cardinal (horizontal and vertical) orientations than to oblique orientations. However, electrophysiological results from the macaque monkey visual cortex are controversial. Both isotropic and anisotropic orientation distributions have been reported. It is also unclear whether different visual areas along the visual hierarchy have different orientation anisotropies. We analyzed orientation maps in a large set of intrinsic signal optical imaging data and found that both V1 and V4 exhibited significant orientation anisotropies. However, their overrepresented orientations were very different: in V1, both cardinal and radial orientations were overrepresented, while in V4, only cardinal bias was presented. These findings suggest that different cortical areas have evolved to emphasize different features that are suitable for their functional purposes, a factor that needs to be considered when efforts are made to explain the relationships between the visual environment and the cortical representation and between the cortical representation and visual perception.

orientation anisotropy | macaque | ISOI | visual cortex

Significance

Orientation selectivity is one of the most important functional features of visual neurons. In the primate visual cortex, whether all orientations are represented equally is still unclear. Previous electrophysiological recordings led to controversial findings. By analyzing a large set of optical imaging data, we found anisotropic representations of orientation in macaque visual areas and that different areas had different types of anisotropies. These findings not only shed light on the long-standing question regarding a basic property of the primate visual cortex, but also on the strategy the visual system takes to represent and analyze the visual world.

Orientation selectivity is a fundamental property of visual neurons in early visual cortices. Since the initial study by Hubel and Wiesel, orientation selectivity has now been described in detail. An interesting phenomenon is that there are anisotropic orientation representations in visual cortices of mammals. In the ferret and the cat V1, for example, there are more neurons preferring horizontal and vertical orientations than neurons preferring oblique orientations, namely, cardinal bias or oblique effects (Fig. 1*C*) (1, 2).

To date, it remains controversial whether orientation anisotropy exists in macaque visual cortices. Previous studies have examined this issue with electrophysiological recordings and reported either no anisotropy (3, 4) or strong anisotropies (5–7) in V1. Such inconsistency may be due to the limitation of the single-cell recording technique: To examine the populational distribution, a large sample of neurons is needed to avoid contributions from random factors. Compared with electrophysiology, population-response–based optical imaging has been proven to be an effective way to measure orientation anisotropy in cats (8–12), ferrets (3, 13–15), and owl monkeys (16). However, to our knowledge, no systematic analysis of orientation anisotropy has been reported for orientation maps in macaque visual areas.

In the macaque visual cortex, orientation selectivity has been described in both lower (e.g., V1, V2) and higher (e.g., V4) visual areas. Whether the orientation anisotropies are the same in these areas remains unclear. In particular, area V4 is crucial for object recognition (17). Compared with V1, orientation representation in V4 is more complex and closer to perception. A better understanding of the orientation anisotropy along this object recognition pathway is important to study hierarchical visual information processing.

In cats and ferrets, cardinal orientation biases have been frequently reported. In addition, some studies reported a correlation between the receptive field (RF) location and the overrepresented orientation [i.e., more neurons tended to prefer orientations connecting their RFs and the point of foveal fixation, a phenomenon called "radial bias" (18–20)]. Fig. 1 illustrates models of three types of anisotropic distributions: cardinal bias, radial bias, and a combination of these two. Overrepresentations were modeled with circular Gaussian functions. For cardinal bias (Fig. 1*C*), the distributions from the left- and right-hemispherical visual cortex (corresponding to the right and left visual fields) were identical. For the radial and combined models (Fig. 1 *D* and *E*), the distributions from the left and right visual cortices are different but symmetrical about the 90° orientation.

We analyzed a large number of orientation maps obtained with intrinsic signal optical imaging (ISOI) from macaque visual cortices and found clear orientation anisotropies in areas V1 and V4. These two areas have different anisotropies: The distribution in V1 needs to be explained with a combined model, and V4 appears to be a pure cardinal bias with a larger amplitude than V1.

Author affiliations: [a]State Key Laboratory of Cognitive Neuroscience and Learning, IDG/McGovern Institute for Brain Research, Beijing Normal University, Beijing 100875, China

Author contributions: C.F. and H.D.L. designed research; C.F. and X.C. performed research; C.F. analyzed data; C.F. and H.D.L. interpreted the results; and C.F. and H.D.L. wrote the paper.

The authors declare no competing interest.

This article is a PNAS Direct Submission.

[1]To whom correspondence may be addressed. Email: haidong@bnu.edu.cn.

This article contains supporting information online at http://www.pnas.org/lookup/suppl/doi:10.1073/pnas.2113407119/-/DCSupplemental.

Published April 5, 2022.

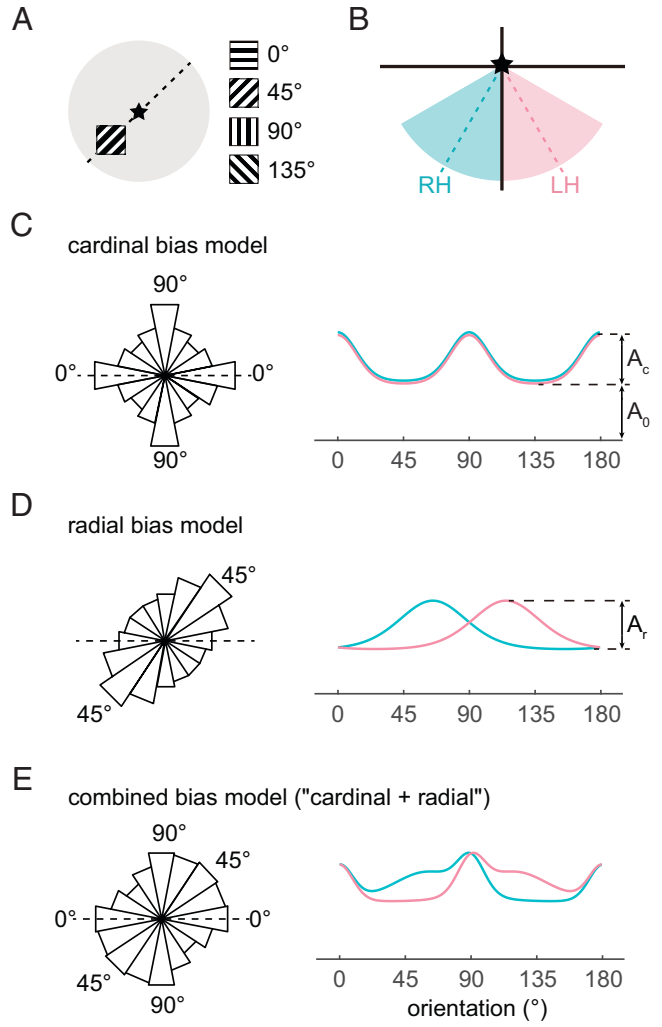

Fig. 1. Illustration of three types of orientation anisotropies. (*A*) Illustration of the four grating stimuli used in the present study and one that is presented at the lower left visual field. Black star represents the fovea. The dashed line represents the radial angle (45°) of the location that the stimulus presents. (*B*) The left and right lower visual field regions and their mean radial angles (dashed lines) corresponding to the right hemisphere (RH, cyan, same below) and left hemisphere (LH, pink, same below) visual cortices imaged in this study. (*C*–*E*) Three types of orientation bias models. (*C*) The cardinal bias model, in which more neurons prefer horizontal (0°) and vertical (90°) orientations than oblique orientations. *Left* is a polar plot of the distribution. Dashed line represents 0° orientation. *Right* is a Cartesian plot of similar distributions on the left, in which left- and right-hemispherical distributions are plotted in different colors as in *B*. In this model, orientation anisotropy is independent of retinotopic location and thus is identical for distributions from the left and right hemispheres. The amplitude of the cardinal anisotropy is denoted as A_c. A_0 represents the baseline. (*D*) The radial bias model, in which more neurons prefer the orientation pointing toward the foveal fixation (radial angle; e.g., 45° for the stimulus location in *A*). *Right* plots the preferred orientation distributions of the left and right hemispheres shown in *B*, which are symmetrical about the 90° orientation. Note that since the radial angle varies with the cortical locations, each peak of the distribution represents a sum of a range of radial angles. A_r represents the amplitude of the radial bias. (*E*) The combined model is a linear summation of cardinal and radial biases. The shape of the distribution depends on both the location of the visual field under examination and the relative strengths of the two components.

Results

ISOI data were from previous experiments in the laboratory and were all collected from anesthetized macaques with a typical imaging paradigm as described in earlier studies (21, 22). Fig. 2*A* illustrates an example right-hemisphere V1 case, which had a visual representation in the lower left visual field. The stimuli were large field square-wave gratings drifting in eight equally spaced directions (four orientations) (Fig. 1*A*). Four single-orientation maps were obtained with a support vector machine (SVM) method comparing cortical responses to gratings and a blank screen (*SI Appendix*, Fig. S1 *E*–*H*). The four maps were then filtered with a bandpass filter after Fourier frequency analysis (*SI Appendix*, Fig. S2 *A*–*D*). A polar map of orientation preference (e.g., Fig. 2*B*) was calculated by vector summing of the four single-orientation maps. Each color in the polar map represents one preferred orientation, in the range of 0° to 180°.

Based on the polar map, a distribution of preferred orientation was calculated by pooling all V1 pixels into 18 bins between 0° and 180°. The three panels in Fig. 2*D* show the data distribution (black dots and dotted lines, same for the three panels) and the best-fitting curves (colored lines) of three different models. Each data point in the distribution represents the percentage of the pixels that had preferred orientation located in the corresponding 10° orientation bin. The cardinal model (*Top*) was composed of two identical circular Gaussian functions peaked at 0° and 90°. The radial model (*Middle*) contained a single circular Gaussian whose peak location was determined by averaging the radial angles of all the V1 pixels (Fig. 2*C* and *SI Appendix*, Fig. S3 *I* and *J*). The combined model (*Bottom*) was a linear summation of the cardinal and radial components described above. Fig. 2*D* shows that the cardinal model could not fit the data (adjusted $R^2 = 0.15$). While the radial model had a better fitting (adjusted $R^2 = 0.47$), it did not reflect the multiple peaks in the data. The combined model captured all the main features of the data distribution and fit the data best (adjusted $R^2 = 0.92$).

We further examined a V4 case with the same method. This right-hemisphere V4 had a visual field representation similar to the V1 case and was located in the contralateral lower visual field (Fig. 2*G*). Fig. 2*H* shows that the V4 orientation distribution was also anisotropic. The peaks were located at 0° and 90° cardinal orientations. In the three fitting models, the cardinal and combined models had similar fitting goodness (adjusted $R^2 = 0.81$ and 0.77, respectively). In contrast, the radial model could not fit the data (adjusted $R^2 = -0.06$). Thus, the orientation preferences in this V4 case showed mainly a cardinal bias. Two single-case examples from V1 and V4 showed distinct orientation anisotropies.

We analyzed 48 hemispherical V1 data (i.e., 48 cases) from 36 animals. The radial angles were determined individually for each case (*SI Appendix*, Fig. S3*K*), similar to the example (Fig. 2*C*). Fig. 3*A* shows the averaged left- ($n = 26$, pink) and right-hemisphere ($n = 22$, cyan) data and the averages of their fitted curves (combined model). Both data distributions had two common cardinal peaks (~0° and 90°) and a unique third peak at ~60° (for right-hemisphere V1) or 120° (for left-hemisphere V1). The two hemispherical data distributions had significant differences around their radial peaks (asterisks in Fig. 3*A*, $P < 0.01$, Wilcoxon rank sum test with Bonferroni correction). The locations of these differences were consistent with the prediction of the combined model. Additionally, left- and right-hemispherical distributions were similar in terms of their anisotropic amplitudes and fitting goodness (*SI Appendix*, Fig. S4 *C* and *E*–*G*), indicating homogeneity in V1 anisotropy in the lower visual field.

We flipped all the left V1 distributions horizontally (about the 90° orientation line) and treated them as right-hemispherical V1 distributions. The flipped left-V1 data and right-V1 data were not different at any orientation bin ($P > 0.20$, Wilcoxon rank sum test with Bonferroni correction). Fig. 3*B* shows the averaged

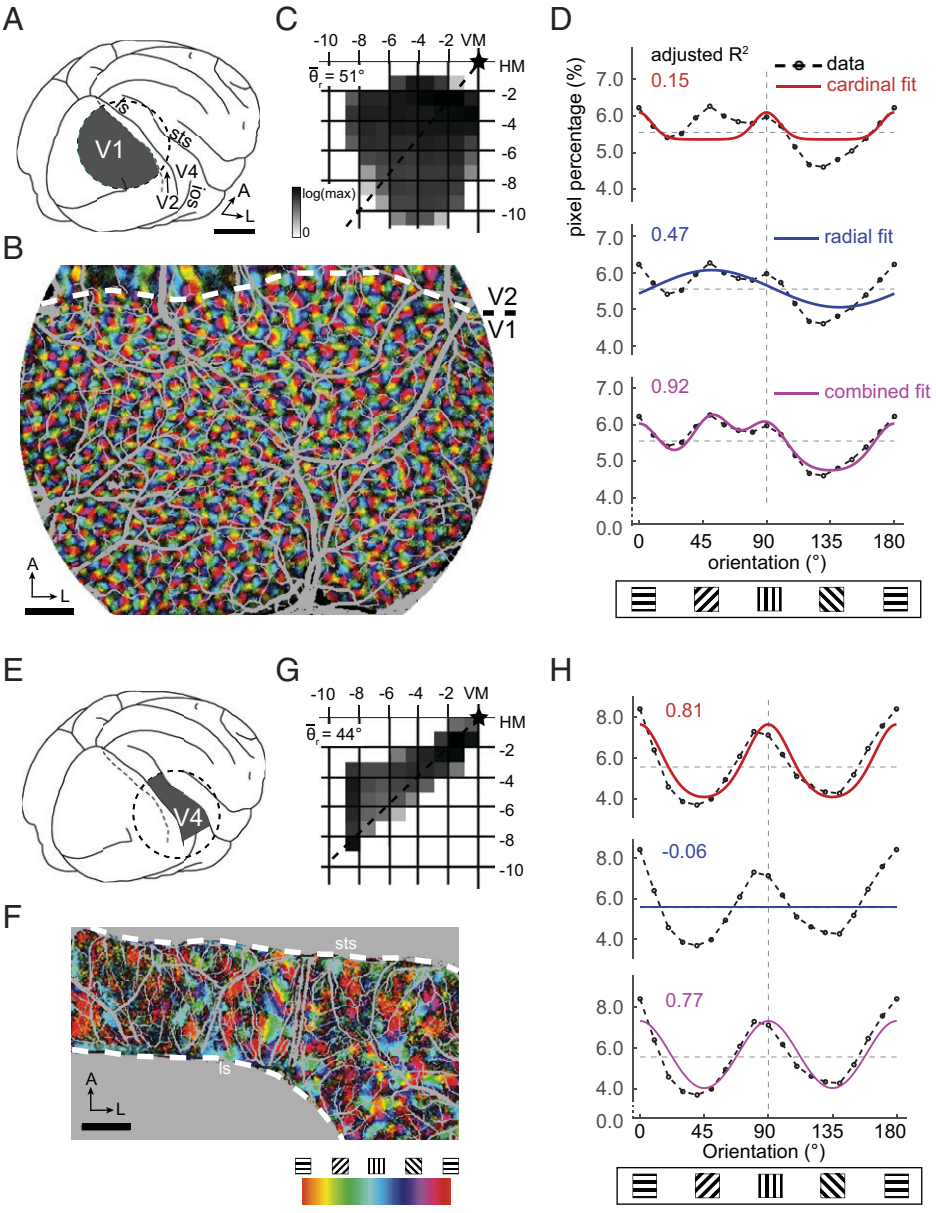

Fig. 2. Single-case orientation anisotropy in V1 and V4. (*A*) Illustration of a typical V1 imaging chamber location (dashed circle) and regions of V1 being analyzed (shading). Scale bar, 10 mm. A, anterior; L, lateral; sts, superior temporal sulcus. (*B*) An example V1 orientation polar map, based on vector summing of four single-orientation maps (*SI Appendix*, Fig. S1 *E–H*), in which different colors represent different preferred orientations. The color index is shown under *F*. Blood vessel pixels (gray) were excluded from the calculation. Scale bar, 2 mm. (*C*) The visual field represented by V1 shown in *B*. Black star represents the fovea. Darkness represents the logarithmic number of pixels. The oblique dashed line represents the mean radial angles of these pixels ($\bar{\theta}_r = 51°$) (*SI Appendix*, Fig. S3 *I* and *J*). HM, horizontal meridian. (*D*) The orientation distribution calculated from the polar map shown in *B* (dotted curves, same in three panels) and three types of fitting curves (colored curves). Each data point represents a percentage of the pixels preferring orientations within the 10° bin (±5°). Goodness of fit (adjusted R^2) is labeled for each model. The horizontal dashed lines represent the uniform distribution (5.56%). Vertical dashed line represents 90° orientation. (*E–H*) A single case example of a right-hemispherical V4 using the same plot conventions as in *A–D*.

V1 data distribution and combined model fitted curve ($n = 48$). A repeated-measures ANOVA indicated a significant main effect of orientation ($F_{4.65,\ 213.90} = 13.35$, $P < 0.001$, with Greenhouse-Geisser correction). Further model analysis revealed that the combined model provided the best fitting among the three models (*SI Appendix*, Fig. S4 *H–J*).

The combined model was a linear sum of cardinal and radial components and a baseline value A_0 (i.e., $D = A_cD_c + A_rD_r + A_0$). The cardinal and radial components are plotted in Fig. 3*C*. The amplitudes of the radial components ($\bar{A}_r = 0.91\%$) were larger than the amplitudes of the cardinal components ($\bar{A}_c = 0.61\%$) ($P < 0.01$, pairwise t test). The mean peak-trough difference of the combined model was 0.98%, which was 17.69% of the mean value (100%/18 = 5.56%) in a uniform distribution, indicating that the orientation anisotropy in V1 made a 17.69% modulation over the uniform distribution. The cardinal and radial components modulated 10.90% and 14.83%, respectively. To estimate the random effects in the orientation distributions, we calculated a shuffled distribution (gray in Fig. 3*B*) for each case, in which the four orientation values for all the pixels were randomly shuffled. The mean shuffled distribution was mainly flat ($F_{4.65,\ 213.90} = 1.37$, $P = 0.19$, repeated-measures ANOVA with Greenhouse-Geisser correction).

Fig. 3*G* shows the scatter plot of A_r and A_c for all V1 cases. Large case variations can be observed. Many cases had $A_c = 0$, but few cases had $A_r = 0$. Both A_r and A_c were larger than the values calculated from the shuffled data (A_c-V1 vs. A_c-V1-shuffle, A_r-V1 vs. A_r-V1-shuffle, $P < 0.001$, two-way ANOVA followed

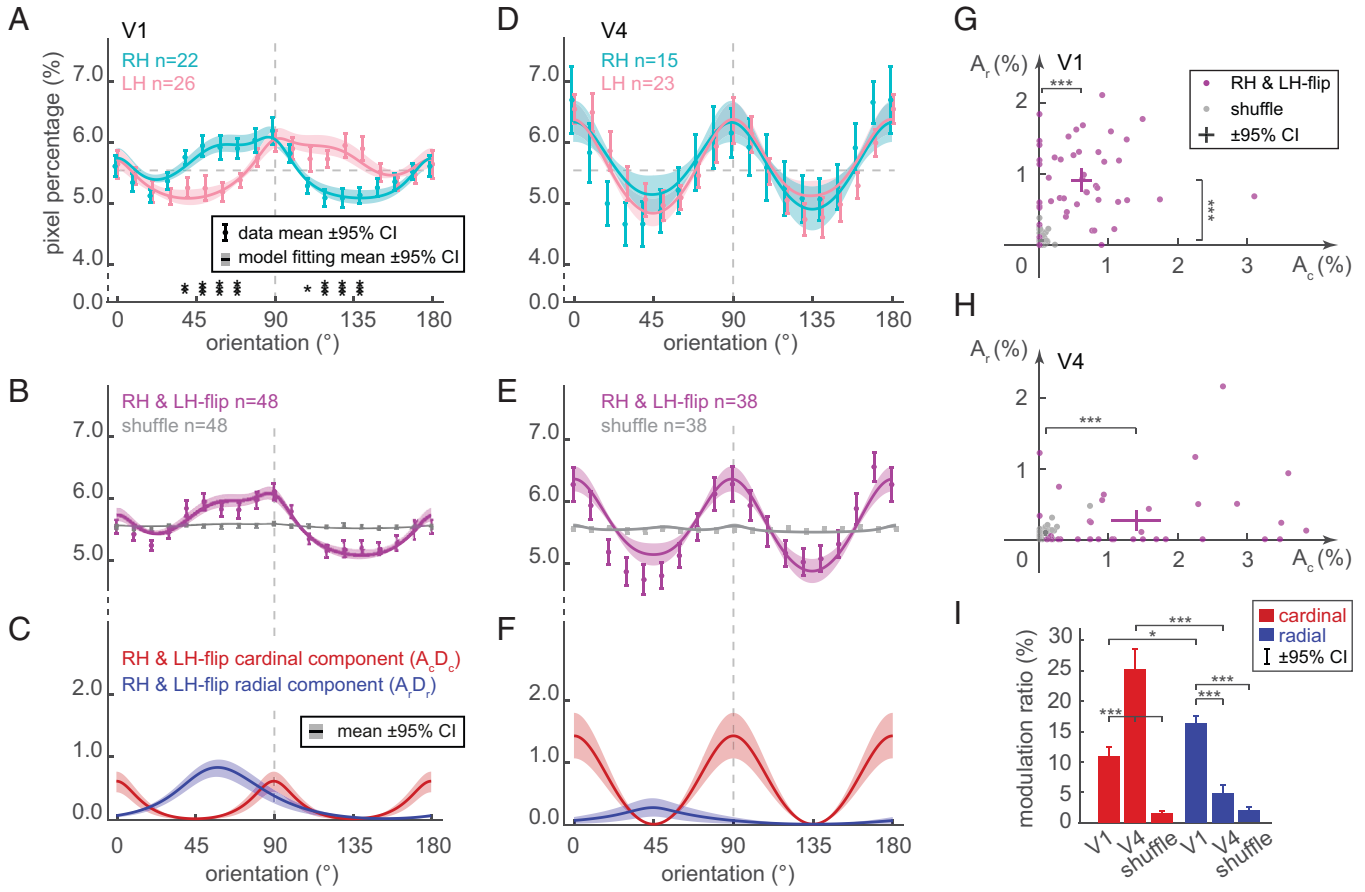

Fig. 3. V1 and V4 population results and fittings of the combined model. (*A*) The mean distributions of preferred orientations for left-hemisphere (LH, pink, $n = 26$) and right-hemisphere (RH, cyan, $n = 22$) V1 cases (data points) and the means of their fittings by the combined model (curves). The horizontal dashed line represents the uniform distribution (5.56%). The vertical dashed line represents 90° orientation. Asterisks at the *Bottom* of the plot represent significant differences between LH and RH distributions at each orientation bin (*$P < 0.05$; **$P < 0.01$; ***$P < 0.001$; symbol representation is the same in the article; Wilcoxon rank sum test with Bonferroni correction). Error bar: 95% CI, curve shading: 95% CI (same below). (*B*) The mean orientation distribution of all V1 cases (purple, $n = 48$), in which every left-hemisphere V1 distribution was flipped horizontally (about the 90° axis, vertical gray dashed line) and treated as right-hemisphere V1 data. Plot conventions same as in *A*. Gray data points and solid gray line represent the distribution of a shuffled control (see *Materials and Methods*). (*C*) The mean cardinal and radial components of V1 combined model fittings. (*D–F*) Similar to *A–C*, for V4 cases. (*G*) Distribution of amplitudes of cardinal and radial components (A_c and A_r) for V1 cases and their shuffled control shown in *B*. The mean and 95% CI are indicated by "+". Asterisks represent the significant differences between V1 and its shuffled control (*$P < 0.05$; ***$P < 0.001$, two-way ANOVA followed by Bonferroni post hoc tests, same in *G–I*). (*H*) Similar to G, for V4 cases. (*I*) Cardinal and radial modulation ratios in V1 and V4, calculated with the formulas $A_c/(100/18)$ and $A_r/(100/18)$.

by Bonferroni post hoc tests). Overall, these cases do not form separate clusters/groups.

For area V4, we analyzed 38 hemispheres from 34 animals. In contrast to the V1 data, both left-and right-hemispherical V4 distributions had two common cardinal peaks but lacked the third (radial) peak (Fig. 3*D*). The comparisons of the fitting results showed no significant difference between the two hemispheres (in fitting goodness and anisotropic amplitudes, *SI Appendix*, Fig. S4 *D–G*). We also flipped left-V4 distributions around the 90° axis and treated them as right-V4 data (Fig. 3*E*). A repeated-measures ANOVA indicated a significant main effect of orientation ($F_{4.45,\ 160.16} = 19.90$, $P < 0.001$, with Greenhouse-Geisser correction). The fitting goodness values showed that both cardinal and combined models well explained the distributions, which were better than the radial model (*SI Appendix*, Fig. S4 *H–J*). In the combined model, the amplitudes of the cardinal components ($\bar{A}_c = 1.42\%$) were larger than the amplitudes of the radial components ($\bar{A}_r = 0.27\%$) ($P < 0.001$, pairwise t test, Fig. 3*H*). Comparisons between V4 and V4 shuffles showed a significant difference in cardinal components (A_c-V4 vs. A_c-V4-shuffle, $P < 0.001$) but not in radial components (A_r-V4 vs. A_r-V4-shuffle, $P = 1.00$, two-way ANOVA followed by Bonferroni post hoc tests). The combined model revealed that the mean peak-trough difference was 1.47%, which was a 26.39% modulation over the uniform distribution, including 25.34% cardinal and 4.75% radial modulations. The above analysis was based on all pixels in V4, and we also repeated the same analysis with V4 pixels showing strong orientation preferences and reached the same conclusion (*SI Appendix*, Fig. S5).

Comparing V1 and V4, V4 had a larger cardinal component than V1 (A_c-V1 vs. A_c-V4, $P < 0.001$) and a weaker radial component (A_r-V1 vs. A_r-V4, $P < 0.001$, two-way ANOVA followed by Bonferroni post hoc tests, Fig. 3*I*). Thus, the orientation anisotropy of V4 is different from the orientation anisotropy of V1 in both anisotropic type and amplitude.

We examined whether sex (male vs. female) and species (*Macaca mulatta* vs. *Macaca fascicularis*) might have effects on orientation anisotropies. The results showed no significant difference between these subgroups in anisotropic amplitudes (*SI Appendix*, Fig. S6 *A–H*). We further examined the effect of visual field eccentricity on orientation anisotropy, in which we separated pixels according to their average eccentricity. Results showed that eccentricity does not affect anisotropic components in V1 and V4 (*SI Appendix*, Fig. S6 *I–L*).

In our V1 cases, many had V2 exposed on surface. The exposed V2 was relatively small, with an average width of

2 mm (range, 0 to 8 mm), representing a visual field around the lower vertical meridian (VM) (*SI Appendix*, Fig. S7 *A* and *B*). We analyzed the cases with more than 2 mm V2 exposed (V2-VM, 51 cases in 35 animals) and found that their orientation distributions had two peaks at 0° and 90° cardinal orientations. The 90° peak was higher than the 0° peak, representing a linear summation of cardinal and radial biases (*SI Appendix*, Fig. S7 *C–E*). This phenomenon was similar to the distributions of V1 regions having comparable visual fields (V1-VM, *SI Appendix*, Fig. S7 *F–J*). Similar to V1, the combined model fit the V2 distributions best (*SI Appendix*, Fig. S7*K*). V2-VM had a larger cardinal component but a radial component similar to V1-VM (*SI Appendix*, Fig. S7*L*). Based on these limited data, it seems that V2 exhibits both cardinal and radial biases.

In the above analysis, we pooled all pixels in each case and used the mean radial angle as a representative for these pixels. We also confirmed that the combined model is suitable for any cortical region with a specific radial angle (*SI Appendix*, Fig. S8).

Discussion

By examining a large set of ISOI data, we found that both macaque V1 and V4 had clear orientation anisotropies. Fig. 4 summarizes our findings. For V1, orientation anisotropy contained both visual field location-independent (cardinal) and location-dependent (radial) components. Their combined effect was a 17.69% modulation over the otherwise uniform distribution. In contrast, V4 exhibited a typical cardinal orientation anisotropy, which had a 26.39% modulation effect. Analysis results from subgroups (e.g., left- and right-hemisphere data, different eccentricities) also yielded consistent results. Since our data were all from the cortex representing the lower visual field, our conclusions are restricted to the lower visual field.

ISOI Method Considerations. Unlike previous approaches in studying orientation distributions in macaques, the present study addresses this issue with an optical imaging method. ISOI measures the population responses and effectively overcomes the sampling problems in electrophysiological recording. The ISOI signal is an indirect measure of neural activity and has several limitations despite its advantages in this specific task. For example, ISOI signals mainly represent neural responses in the superficial layers. However, due to the columnar organization of orientation preferences, it is very likely that deep layers have anisotropies similar to those of the superficial layers. Additionally, the hemodynamic signal is the sum of responses from a large population of neurons and thus does not reveal the tuning width and strength of individual neurons. In our data analysis, we limited our focus to the preferred orientation of pixels and did not consider the tuning strength (except in *SI Appendix*, Fig. S5). The main purpose of this limit in focus was to include as much data as possible to overcome the low signal-to-noise ratio problem. The orientation distribution was presented as pixel numbers (i.e., proportion of cortical surfaces) and thus is approximately proportional to neuron numbers.

Similar to the procedures in previous studies (10, 14, 23), we bandpass-filtered the single-condition maps and only analyzed middle-frequency signals. The low- and high-frequency components are believed to be mostly noise and do not relate to the domain-level orientation signals we studied. We analyzed the maps in low-, middle-, and high-frequency ranges separately and evaluated the stimulus orientation information they each contained. Linear classifier analyses based on stimulus

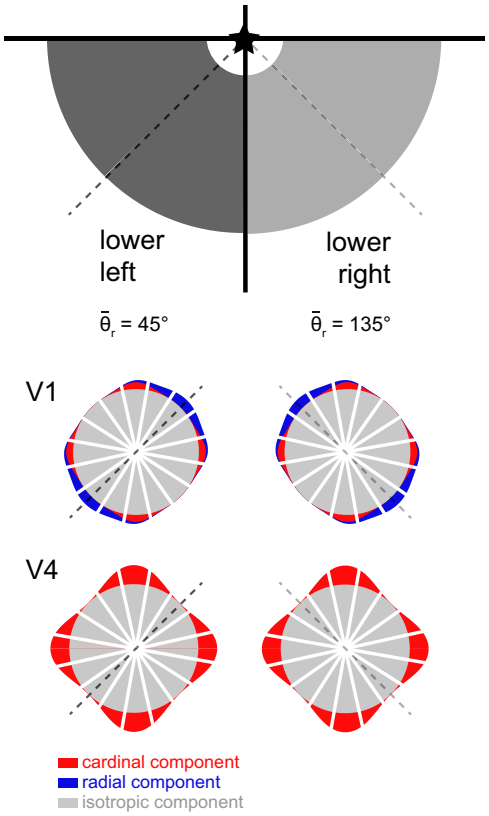

Fig. 4. Illustration of orientation anisotropies in macaque V1 and V4. The figure illustrates V1 and V4 anisotropic types and amplitudes. The lower visual field is divided into left (dark) and right (light) quadrants, which correspond to the right and left hemispheres, respectively. Black star represents the fovea. Dashed lines represent mean radial angles, which are 45° and 135° for the lower left and lower right, same below. The red, blue, and gray fillings represent cardinal, radial, and isotropic components. For the lower visual field, V1 contains an overrepresentation of orientations in both cardinal (horizontal and vertical) and radial axes. V4 contains an overrepresentation of orientations along the cardinal axes only.

orientation were performed on the low-, middle-, and high-frequency single-orientation maps (*SI Appendix*, Fig. S2*J*). For the high-frequency component, the decoding accuracies were near 25% (chance level) for both V1 and V4, which means that they did not carry any orientation information. For the middle frequency component, the accuracies were close to 100%. For the low-frequency component, the rates were ∼60%, which were higher than chance, indicating that low-frequency maps do contain some orientation information. However, these maps had lower decoding accuracy (*SI Appendix*, Fig. S2*J*) and very poor fitting goodness (*SI Appendix*, Fig. S2*L*). In addition, the orientation distributions obtained from low-frequency components had high SDs (*SI Appendix*, Fig. S2 *F* and *K*). Thus, we focused our analysis on the middle-frequency component.

In this study, the orientation responses were measured with gratings presented at four different orientations (spaced at 45°). Without vector summation, anisotropy can be detected from the original V4 data but not for the V1 data (*SI Appendix*, Fig. S9 *A* and *B*), probably due to the differences between their anisotropy types and strengths (Fig. 3*I*). In our main results, preferred orientations of pixels were reconstructed (vector summation) based on these four response values. Limited stimulus orientations have been shown to affect the accuracy of the reconstructed preferred orientations (24). We estimated the errors during the reconstruction procedures and found that the error does not change with the preferred orientation and

thus will not affect the bias in the distribution if it exists (*SI Appendix*, Fig. S9*I*). We further tested the four-sample method on orientation tuning curves drawn from a theoretical orientation distribution with different levels of anisotropy amplitudes. The results show that the sensitivity of anisotropy detection is adequate for the levels of anisotropy amplitude we actually observed in both V1 and V4 (*SI Appendix*, Fig. S9 *J* and *K*).

Relevance to Previous Findings. Orientation anisotropy has been observed in the visual cortex of many mammals, including mice (25–27), ferrets (3, 13–15), cats (2, 8–12, 28, 29), monkeys (1, 4–6, 16, 30, 31), and humans (19, 32–37). The majority of studies observed a cardinal bias in the primary visual cortex. However, many of these studies did not consider visual field locations, making location-dependent radial bias harder to detect. It is possible that the actual anisotropy type is a combination of cardinal and radial biases.

Our V1 results show both cardinal and radial biases. Recent functional MRI (fMRI) studies of human V1 also suggest a combined anisotropy (33–35, 37). A recent study imaged neurons in macaque V1 with two-photon techniques (31). They found a radial bias [i.e., differences between radial and tangential orientations (figure 5C in ref. 31] but no cardinal bias. Although they analyzed more than 10,000 V1 neurons, these neurons were from seven imaging regions, each smaller than 1 mm^2. Due to the presence of orientation domains, large variance among regions was observed (figure 5A in ref. 31). It is possible that more imaging regions may be needed to reveal the cardinal bias we observed. In cats and primates, retinal ganglion cells already exhibit radial bias (38, 39). There is also evidence that radial bias is present in lateral geniculate nucleus (LGN) of the thalamus (40, 41).

For V2, previous recordings have shown either weak anisotropy for vertical orientations (42) or combined cardinal and radial biases (4). Although our V2 data are limited to cortical regions representing the visual field around the lower VM, the results show a clear orientation anisotropy that is similar to the orientation anisotropy in V1, which is a combination of cardinal and radial biases (*SI Appendix*, Fig. S7).

For V4, only a few studies have examined its orientation anisotropy. One fMRI study found that all macaque retinotopic visual areas (V1, V2, V3, and V4) exhibited radial bias. However, the V4 signals appeared less significant than in V1 to V3 (19). In human fMRI studies, a weaker radial bias in V4 compared with V1 to V3 was also reported (19, 33). In our optical imaging data, we found a strong and predominant cardinal bias in V4. Thus, the discrepancy between our and fMRI results needs to be further examined.

For each area, we found a large intercase variability (e.g., Fig. 3 *G* and *H*) similar to what was observed previously in monkeys (4) and ferrets (13), also suggesting that a large sample is important for this type of study.

Implications of the Observations. We observed different anisotropies in V1 and V4. One possibility is that different orientation representations in V1 and V4 are suitable for different purposes. Since V1 is the first stage of cortical visual processing, it is important to faithfully represent the orientation anisotropy in the natural environment, which contains both cardinal and radial abundances (28, 43–45). A realistic representation in V1 may not be directly related to higher-level visual perception but contains all the necessary information for subsequent analysis (e.g., for dorsal and ventral processing). Area V4 may selectively receive partial orientation information from V1 [through V2 pale stripes (46)] and is designed to emphasize the orientations that are important for object recognition (17). Human scene-selective area (the parahippocampal place area, PPA) exhibits clear preferences for cardinal orientations, which is in line with this hypothesis (36).

Another possibility is that, unlike V1 neurons, which mainly code local orientations at object edges, neurons in V4 may tend to code the orientation of individual objects. The abundance of these two types of orientation can be different in the natural environment. For objects, vertical or horizontal positions are apparently more stable and more commonly observed (43). The orientation of local edges, however, has fewer restrictions. Thus, orientation anisotropies in different visual areas are adapted to the unique contribution of the areas to perception or action and may not necessarily be the same.

Materials and Methods

Subjects and Data. All data were from the imaging database of the laboratory and were collected in the past 12 y. Data used in this study came from 79 hemispheres of 58 adult macaque monkeys (45 *M. mulatta*, 14 *M. fascicularis*). All the orientation response maps used in this study were from the first imaging of each case immediately after craniotomy, in which data have a higher signal-to-noise ratio and larger cortical exposure. All procedures were performed in accordance with the NIH Guidelines and were approved by the Institutional Animal Care and Use Committee (Institute of Neuroscience, Chinese Academy of Sciences, and Beijing Normal University).

Surgery. Surgery procedures have been described in detail in previous publications (22, 47). Briefly, monkeys were artificially ventilated and anesthetized with isoflurane (1 to 3%). Anesthetic depth was assessed continuously by monitoring heart rate, end-tidal CO_2, blood oximetry, and body temperature. In most cases, a circular craniotomy (18- to 25-mm diameter) was performed. In four cases, a rectangular (20- to 24-mm) craniotomy was made. A durotomy was performed to expose visual areas V1-V2 or V1-V2-V4 (e.g., Fig. 2).

Optical Imaging. Imaging procedures were described in detail in previous publications (22, 47). The brain was stabilized with agar (4%) and a cover glass (thickness, 2 to 3 mm). During the imaging session, anesthesia was switched to thiopental sodium (induction, 10 mg/kg; maintenance, 1 to 3 mg/kg/h, intravenously [i.v.]) or propofol (induction 5 mg/kg, maintenance 5 to 6 mg/kg/h, i.v.). Animals were paralyzed (vecuronium bromide; induction, 0.25 mg/kg; maintenance, 0.05 to 0.1 mg/kg/h, i.v.) to prevent eye movement. Pupils were dilated (atropine sulfate 1% or tropicamide 5 mg/mL), and eyes were fit with contact lenses of appropriate curvature to focus on a stimulus screen 57 cm from the eyes. Images of cortical reflectance were acquired (Imager 3001, Optical Imaging Inc.) with 632-nm illumination. Image size was either 504 × 504 or 540 × 654 pixels. Each pixel represented 28 to 48 μm of the cortex. For each trial, imaging started 0.5 s before the stimulus onset and was collected at a 4-Hz frame rate. Each visual stimulus was presented for 3.5 s. The total imaging time for each trial was 4 s, during which 16 frames were imaged. Interstimulus intervals were at least 8 s. Stimulus conditions were displayed in a randomized order, and each was repeated 10 to 50 times.

Visual Stimulus. Visual stimuli were created using ViSaGe (Cambridge Research Systems Ltd.) and displayed on a calibrated 21-inch cathode ray tube (CRT) monitor running at a 100-Hz refreshing rate. The stimulus was a full screen (30 × 40°, V1 $n = 48$, V4 $n = 33$) or a square patch larger than 10° (average 14°, V4 $n = 5$) that fully covered the visual field of the imaged cortex. The use of large stimuli minimized the vignetting effect on orientation (48). Stimuli for obtaining orientation maps were square-wave luminance gratings presented to the two eyes. Gratings were drifted in one of eight equally spaced directions perpendicular to their orientations. The corresponding four orientations were labeled 0° (horizontal), 45° (anticlockwise 45° from 0°), 90°, and 135° (Fig. 1*A*). The spatial frequency (SF) of the gratings was 1 or 1.5 cycles/degree, and the temporal frequency was 4 or 5.33 cycles/s. We also used thin lines to map the visual field locations of the imaged areas (*SI Appendix*, Fig. S3, described in *Retinotopic Mapping*).

SVM. All maps in this study were obtained with linear SVM analysis (49, 50, 51). Compared with subtraction maps, SVM maps have a better signal-to-noise ratio while maintaining the linear relationship of the map signals. We first obtained dR/R images for each stimulus condition using the following formula: $dR/R = (R_{6-14} - R_{1-3})/R_{1-3}$, in which R_{6-14} is the average of frames 6 to 14 and R_{1-3} is the average of frames 1 to 3. dR/R images of each stimulus condition and blank condition were then compared by SVM (41, MATLAB, LIBSVM). An optimal classifier was obtained after fivefold cross-validation. The weight map of the trained SVM classifier was used as the "single-condition" map, in which a pixel value represents the contribution of the pixel to the classification.

Vector summation. Each pair of single-condition SVM maps obtained with stimuli moving in opposite directions was averaged, resulting in four "single-orientation" maps. Two-dimensional Fourier analysis was performed, after which bandpass filtering was performed (23). The high-frequency component (high-cutoff: 1/6 cycle/pixel, average five cycles/mm) and low-frequency component (low-cutoff: 1/3 cycle/mm) were removed. Four single-orientation maps were pixelwise vector-summed (52, 53), resulting in two vector component maps: an angle map representing the preferred orientation (0 to 180°) of each pixel and another magnitude map representing the magnitude of the orientation preference.

Regions Analyzed. The V1/V2 borders were determined with ocular dominance (53) or orientation imaging. For area V1, its medial and posterior borders were usually the craniotomy borders. Laterally, we excluded the foveal region (<1° eccentricity) since its orientation map was usually weak (probably due to the relatively low SF grating we used). Anteriorly, the V1 border was either the V1/V2 border or the lunate sulcus (ls). V2 was usually a narrow band between V1 and the ls. We only analyzed cases with V2 exposures wider than 2 mm. In the V1 and V2 comparison analysis (*SI Appendix*, Fig. S7), we only analyzed regions within 3 mm on each side of the V1/V2 border. For V4, the anterior and posterior borders were the superior temporal sulcus and ls, the lateral border was the inferior occipital sulcus (ios), and the medial border was the craniotomy border.

Regions of Different Eccentricities. To study the orientation anisotropy at different foveal eccentricities, we divided the V1 or V4 pixels into two parts according to their average eccentricity (5.6° for V1 and 5.2° for V4).

Distribution of Preferred Orientation and Fitting Models. A distribution of preferred orientation (e.g., Fig. 2*D*, black) was calculated based on the angle map from the vector summation analysis. All pixels were allocated into 18 bins between 0 and 180° (e.g., all pixels with angle values between 85° and 95° were allocated into the 90° bin). Since a small pixel number causes a large deviation, in subregion comparisons the distribution calculated with a pixel number smaller than 10,000 was excluded. Next, we examined the fitting goodness of three distribution models: cardinal-bias model, radial-bias model, and cardinal-radial–combined model. The core functions of these models were all von Mises functions (i.e., circular Gaussian). Then, the fitting was calculated with the nonlinear least squares algorithm in MATLAB (fitnlm). The cardinal bias model is

$$D = A_c D_c + A_0 = a_c\left(e^{b_c\cos(2\theta)} + e^{b_c\cos(2(\theta-90°))}\right) + A_0, \quad [1]$$

$$A_c = a_c\left(e^{b_c} + e^{-b_c}\right) - 2a_c. \quad [2]$$

The radial bias model is

$$D = A_r D_r + A_0 = a_r e^{b_r\cos(2(\theta-\theta_r))} + A_0, \quad [3]$$

$$A_r = a_r\left(e^{b_r} - e^{-b_r}\right). \quad [4]$$

The "cardinal + radial" combined bias model is

$$D = A_c D_c + A_r D_r + A_0 = a_c\left(e^{b_c\cos(2\theta)} + e^{b_c\cos(2(\theta-90°))}\right) + a_r e^{b_r\cos(2(\theta-\theta_r))} + A_0, \quad [5]$$

in which a_c, a_r, b_c, and b_r determine the amplitude of the peak, and b_c and b_r determine the width of the peak. We used A_c and A_r to represent the amplitude of the curve, which was calculated in functions (2) and (4). D_c and D_r represent the curves after normalization, and A_0 represents the baseline of the curve, which is equal at all orientations. θ represents the preferred orientation and is the only variable (0 to 180°). θ_r is the peak angle of the radial bias and was obtained by averaging the radial angles of all pixels, which was not a predictor variable. The radial angle for each pixel was determined by retinotopic mapping or our estimation (*SI Appendix*, Fig. S3, described in *Retinotopic Mapping* below). All predictor variables (a_c, a_r, b_c, b_r, and A_0) were restricted to values larger than 0.

We mainly used adjusted R^2 to evaluate the fitting goodness:

$$\text{adjusted } R^2 = 1 - \left(\frac{n-1}{n-v}\right)\frac{\sum_{k=1}^{n}(y_k - \hat{y}_k)^2}{\sum_{n=1}^{n}(y_k - \bar{y})^2}, \quad [6]$$

in which y_k ($k = 1, 2 \ldots, n$, n represents the number of bins, which is 18) is the original data values and $\bar{y}$ is the average of these values. $\hat{y}_k$ ($n = 1, 2 \ldots, n$) is the values from fitting, v is the number of predictor variables, which is 3 for the cardinal and radial models and 5 for the combined model. The adjusted R^2 adjusts for the number of predictor variables in the model, which makes it appropriate for comparing models with different numbers of predictors. Larger adjusted R^2 means better fitting. We also used the Akaike information criterion (AIC) and likelihood ratio test (LRT) to double-check the fitting goodness:

$$AIC = -2LL(\text{model}) + 2v, \quad [7]$$

$$\chi^2 = 2(LL(\text{combinded model}) - LL(\text{cardinal or radial model})), \quad [8]$$

where LL( ) represents the log-likelihood. For LRT, the test statistic χ^2 followed an approximate χ^2 distribution of degrees of freedom of difference in number of predictor variables. We tested at a level of significance $\alpha < 0.05$. We used adjusted R^2 to compare the models fitted on both identical and different data. AIC and LRT were confined to compare the models fitted on identical data.

Random Control. To evaluate the potential systematic error in calculating the orientation distribution, we performed the same analysis on shuffled data (Fig. 3 *B* and *E*). For each case, we calculated four new single-orientation maps by shuffling the orientation condition and pixel location of each pixel (i.e., the four orientation values for all the pixels were randomly shuffled). The same vector summation, distribution, and model analyses were then performed on the new shuffled dataset.

Retinotopic Mapping. Retinotopy of the imaged area was measured in 22 V1 cases and 18 V4 cases. The mapping procedures were the same as those described in previous publications (22, 54). A single horizontal or vertical grating strip (typical width: 0.1° to 0.2°, length: 30° to 40°) was presented on the stimulus screen for 3.5 s, and V1 or V4 activation was imaged. The gratings within the strip were square-wave (SF = 1.5 cycles/degree, duty cycle = 0.5), oriented orthogonal to the strip, and drifted along the strip length at 8°/s. Thus, the stimulus looked like a dashed line drifting along the vertical/horizontal direction. This procedure was repeated for different line locations until the entire imaging region was mapped (*SI Appendix*, Fig. S3*D*). The vertical line that activated the V1/V2 border was the VM, and the horizontal line that activated the conjectural ios (usually not in the field of view for V1 imaging) was the horizontal meridian. The retinotopy was then determined based on these activation maps. For cases in which retinotopies were not measured (V1: $n = 26$, V4: $n = 20$), we created standard retinotopic maps to estimate their retinotopies. For V1 cases, we estimated the retinotopic location of each pixel according to its distances between the V1/V2 border and the sagittal suture (*SI Appendix*, Fig. S3*G*). For V4 cases, we estimated the retinotopic location of each pixel according to its distances between ls and the start point of ios (*SI Appendix*, Fig. S3*H*). Finally, maps of all cases were rotated and scaled to fit the standard maps.

Statistics. The Wilcoxon rank sum test was used to detect the differences between distributions at each orientation bin, and their pairwise *P* values were adjusted by the Bonferroni method (e.g., Fig. 3*A*). We used repeated-measures ANOVA followed by Greenhouse-Geisser correction to determine whether orientation had a significant main effect on distribution (e.g., Fig. 3*B*) (11, 31). Two-way ANOVA was used to compare amplitudes of anisotropic components (factor one: cardinal vs. radial) and different conditions (factor two: e.g., V1 vs. V4 vs. shuffle), and their *P* values of post hoc test were adjusted by the Bonferroni method. We compared values between components or conditions but did not mention any comparison between the two (e.g., A_r-V1 vs. A_c-V4) in the study. We also used paired, two-tailed *t* tests followed by Bonferroni correction to compare the goodness of fits, amplitudes, and other values (e.g., *SI Appendix*, Fig. S4).

Data Availability. All single-case data (preprocessed), an example original dataset, and MATLAB code required to reproduce all figures are available at the Open Science Framework (DOI: 10.17605/OSF.IO/GS6CU).

ACKNOWLEDGMENTS. We thank laboratory members (C. Liang, P. Li, H. Ma, Q. Song, R. Tang, J. Wang, K. Yan, R. Zhang) and alumni (M. Chen, Y. Fang, C. Han, J. Hu, P. Li, Y. Li, H. Xu, S. Zhu) who were involved in the data collection. We thank laboratory assistants (J. Lu, Y. Xiao) for their technical assistance. We thank Prof. D.H. Wang for his valuable discussion. This work was supported by the National Natural Science Foundation of China (grants 31625012, 31530029, and 31371111) and the Hundred Talent Program of the Chinese Academy of Sciences.

1. N. E. Berman, M. E. Wilkes, B. R. Payne, Organization of orientation and direction selectivity in areas 17 and 18 of cat cerebral cortex. *J. Neurophysiol.* **58**, 676–699 (1987).
2. D. M. Coppola, L. E. White, D. Fitzpatrick, D. Purves, Unequal representation of cardinal and oblique contours in ferret visual cortex. *Proc. Natl. Acad. Sci. U.S.A.* **95**, 2621–2623 (1998).
3. D. H. Hubel, T. N. Wiesel, Receptive fields and functional architecture of monkey striate cortex. *J. Physiol.* **195**, 215–243 (1968).
4. G. Shen, X. Tao, B. Zhang, E. L. Smith III, Y. M. Chino, Oblique effect in visual area 2 of macaque monkeys. *J. Vis.* **14**, 3 (2014).
5. R. J. W. Mansfield, Neural basis of orientation perception in primate vision. *Science* **186**, 1133–1135 (1974).
6. R. L. De Valois, E. W. Yund, N. Hepler, The orientation and direction selectivity of cells in macaque visual cortex. *Vision Res.* **22**, 531–544 (1982).
7. R. Bauer, B. M. Dow, Complementary global maps for orientation coding in upper and lower layers of the monkey's foveal striate cortex. *Exp. Brain Res.* **76**, 503–509 (1989).
8. F. Sengpiel, P. Stawinski, T. Bonhoeffer, Influence of experience on orientation maps in cat visual cortex. *Nat. Neurosci.* **2**, 727–732 (1999).
9. G. Wang, S. Ding, K. Yunokuchi, Representation of cardinal contour overlaps less with representation of nearby angles in cat visual cortex. *J. Neurophysiol.* **90**, 3912–3920 (2003).
10. L. Huang *et al.*, Slab-like functional architecture of higher order cortical area 21a showing oblique effect of orientation preference in the cat. *Neuroimage* **32**, 1365–1374 (2006).
11. J. Ribot, S. Tanaka, K. O'Hashi, A. Ajima, Anisotropy in the representation of direction preferences in cat area 18. *Eur. J. Neurosci.* **27**, 2773–2780 (2008).
12. T. S. Altavini, S. A. Conde-Ocazionez, D. Eriksson, T. Wunderle, K. E. Schmidt, Selective interhemispheric circuits account for a cardinal bias in spontaneous activity within early visual areas. *Neuroimage* **146**, 971–982 (2017).
13. B. Chapman, T. Bonhoeffer, Overrepresentation of horizontal and vertical orientation preferences in developing ferret area 17. *Proc. Natl. Acad. Sci. U.S.A.* **95**, 2609–2614 (1998).
14. D. M. Coppola, L. E. White, Visual experience promotes the isotropic representation of orientation preference. *Vis. Neurosci.* **21**, 39–51 (2004).
15. A. Grabska-Barwińska, C. Distler, K.-P. Hoffmann, D. Jancke, Contrast independence of cardinal preference: Stable oblique effect in orientation maps of ferret visual cortex. *Eur. J. Neurosci.* **29**, 1258–1270 (2009).
16. X. Xu, C. E. Collins, I. Khaytin, J. H. Kaas, V. A. Casagrande, Unequal representation of cardinal vs. oblique orientations in the middle temporal visual area. *Proc. Natl. Acad. Sci. U.S.A.* **103**, 17490–17495 (2006).
17. A. W. Roe *et al.*, Toward a unified theory of visual area V4. *Neuron* **74**, 12–29 (2012).
18. A. G. Leventhal, Relationship between preferred orientation and receptive field position of neurons in cat striate cortex. *J. Comp. Neurol.* **220**, 476–483 (1983).
19. Y. Sasaki *et al.*, The radial bias: A different slant on visual orientation sensitivity in human and nonhuman primates. *Neuron* **51**, 661–670 (2006).
20. C. W. G. Clifford, D. J. Mannion, J. S. McDonald, Radial biases in the processing of motion and motion-defined contours by human visual cortex. *J. Neurophysiol.* **102**, 2974–2981 (2009).
21. D. Y. Ts'o, R. D. Frostig, E. E. Lieke, A. Grinvald, Functional organization of primate visual cortex revealed by high resolution optical imaging. *Science* **249**, 417–420 (1990).
22. P. Li *et al.*, A motion direction preference map in monkey V4. *Neuron* **78**, 376–388 (2013).
23. D. Y. Ts'o, M. Zarella, G. Burkitt, Whither the hypercolumn? *J. Physiol.* **587**, 2791–2805 (2009).
24. T. Womelsdorf, U. T. Eysel, Z. F. Kisvárday, Comparison of orientation maps obtained with different number of stimulus orientations. *Neuroimage* **13**, 1131–1139 (2001).
25. A. K. Kreile, T. Bonhoeffer, M. Hübener, Altered visual experience induces instructive changes of orientation preference in mouse visual cortex. *J. Neurosci.* **31**, 13911–13920 (2011).
26. M. M. Roth, F. Helmchen, B. M. Kampa, Distinct functional properties of primary and posteromedial visual area of mouse neocortex. *J. Neurosci.* **32**, 9716–9726 (2012).
27. P. G. Fahey *et al.*, A global map of orientation tuning in mouse visual cortex. bioRxiv [Preprint] (2019). https://doi.org/10.1101/745323. Accessed 10 November 2021.
28. V. Dragoi, C. M. Turcu, M. Sur, Stability of cortical responses and the statistics of natural scenes. *Neuron* **32**, 1181–1192 (2001).
29. B. Li, M. R. Peterson, R. D. Freeman, Oblique effect: A neural basis in the visual cortex. *J. Neurophysiol.* **90**, 204–217 (2003).
30. R. Bauer, K. P. Hoffmann, H. P. Huber, M. Mayr, Different anisotropies of movement direction in upper and lower layers of the cat's area 18 and their implications for global optic flow processing. *Exp. Brain Res.* **74**, 395–401 (1989).
31. N.-S. Ju, S.-C. Guan, L. Tao, S.-M. Tang, C. Yu, Orientation tuning and end-stopping in macaque V1 studied with two-photon calcium imaging. *Cereb. Cortex* **31**, 2085–2097 (2021).
32. C. S. Furmanski, S. A. Engel, An oblique effect in human primary visual cortex. *Nat. Neurosci.* **3**, 535–536 (2000).
33. D. J. Mannion, J. S. McDonald, C. W. G. Clifford, Orientation anisotropies in human visual cortex. *J. Neurophysiol.* **103**, 3465–3471 (2010).
34. R. T. Maloney, C. W. G. Clifford, Orientation anisotropies in human primary visual cortex depend on contrast. *Neuroimage* **119**, 129–145 (2015).
35. P. Sun *et al.*, Demonstration of tuning to stimulus orientation in the human visual cortex: A high-resolution fMRI study with a novel continuous and periodic stimulation paradigm. *Cereb. Cortex* **23**, 1618–1629 (2013).
36. S. Nasr, R. B. Tootell, A cardinal orientation bias in scene-selective visual cortex. *J. Neurosci.* **32**, 14921–14926 (2012).
37. J. Freeman, D. J. Heeger, E. P. Merriam, Coarse-scale biases for spirals and orientation in human visual cortex. *J. Neurosci.* **33**, 19695–19703 (2013).
38. J. D. Schall, V. H. Perry, A. G. Leventhal, Retinal ganglion cell dendritic fields in old-world monkeys are oriented radially. *Brain Res.* **368**, 18–23 (1986).
39. W. R. Levick, L. N. Thibos, Orientation bias of cat retinal ganglion cells. *Nature* **286**, 389–390 (1980).
40. S. Ling, M. S. Pratte, F. Tong, Attention alters orientation processing in the human lateral geniculate nucleus. *Nat. Neurosci.* **18**, 496–498 (2015).
41. T. D. Shou, A. G. Leventhal, Organized arrangement of orientation-sensitive relay cells in the cat's dorsal lateral geniculate nucleus. *J. Neurosci.* **9**, 4287–4302 (1989).
42. J. B. Levitt, D. C. Kiper, J. A. Movshon, Receptive fields and functional architecture of macaque V2. *J. Neurophysiol.* **71**, 2517–2542 (1994).
43. D. M. Coppola, H. R. Purves, A. N. McCoy, D. Purves, The distribution of oriented contours in the real world. *Proc. Natl. Acad. Sci. U.S.A.* **95**, 4002–4006 (1998).
44. N. D. B. Bruce, J. K. Tsotsos, A statistical basis for visual field anisotropies. *Neurocomputing* **69**, 1301–1304 (2006).
45. C. A. Rothkopf, T. H. Weisswange, J. Triesch, "Learning independent causes in natural images explains the spacevariant oblique effect" in *2009 IEEE 8th International Conference on Development and Learning* (IEEE, 2009), pp. 1–6. https://doi.org/10.1109/DEVLRN.2009.5175534.
46. F. Chen *et al.*, Function-specific projections from V2 to V4 in macaques. *Brain Struct Funct* 1–14 (2022). https://doi.org/10.1007/s00429-021-02440-3.
47. H. Xu *et al.*, Rivalry-like neural activity in primary visual cortex in anesthetized monkeys. *J. Neurosci.* **36**, 3231–3242 (2016).
48. Z. N. Roth, D. J. Heeger, E. P. Merriam, Stimulus vignetting and orientation selectivity in human visual cortex. *eLife* **7**, e37241 (2018).
49. Y. Xiao, R. Rao, G. Cecchi, E. Kaplan, Improved mapping of information distribution across the cortical surface with the support vector machine. *Neural Netw.* **21**, 341–348 (2008).
50. M. Chen *et al.*, An orientation map for motion boundaries in macaque V2. *Cereb. Cortex* **26**, 279–287 (2016).
51. C.-C. Chang, C.-J. Lin, LIBSVM: A library for support vector machines. *ACM Trans. Intell. Syst. Technol.* **2**, 1–27 (2011).
52. W. H. Bosking, Y. Zhang, B. Schofield, D. Fitzpatrick, Orientation selectivity and the arrangement of horizontal connections in tree shrew striate cortex. *J. Neurosci.* **17**, 2112–2127 (1997).
53. H. D. Lu, G. Chen, H. Tanigawa, A. W. Roe, A motion direction map in macaque V2. *Neuron* **68**, 1002–1013 (2010).
54. H. D. Lu, G. Chen, D. Y. Ts'o, A. W. Roe, A rapid topographic mapping and eye alignment method using optical imaging in Macaque visual cortex. *Neuroimage* **44**, 636–646 (2009).